Mineral Identification and Mapping by Synthesis of Hyperspectral VNIR/SWIR and Multispectral TIR Remotely Sensed Data With Different Classifiers

Li Ni, Honggen Xu, and Xiaoming Zhou

***Abstract*—Hyperspectral data, which have fine continuous spectrum, have been recognized to be more suitable for the detailed identification and classification of land surface, especially for minerals. The combination of the hyperspectral visible/near-infrared (VNIR) and shortwave infrared (SWIR) data with the hyperspectral thermal infrared (TIR) data is proven to be an effective way. However, how those effects are and what are the effects of introduction of multispectral TIR data on the minerals identification and classification are not well studied. To fully evaluate those effects, this article tries to use both simulated data and real data to testify the practicability of introduction of multispectral TIR data for the accuracies of mineral identification and classification. Four classifiers, i.e., spectral angle mapping, spectral feature fitting, orthogonal subspace projection, and adaptive coherence/cosine estimator, are selected in the experiment. Compared with the results using hyperspectral data alone, the introducing of multispectral TIR data in identification and classification has improved accuracies for both the simulated and real data. The overall accuracies are improved about 4%–13% for the simulated data and about 1%–5% for the real data by using different classifiers. Those improvements prove that the spectral diagnosed characteristics in TIR region even for multispectral data help identify and classify minerals. Although the improvements for real data are not well obvious due to the low spatial resolution, the multispectral TIR data are still effective supplements for hyperspectral VNIR and SWIR data in mineral identification and classification.**

***Index Terms*—Classification, emissivity, hyperspectral, thermal infrared (TIR).**

I. Introduction

MINERALS, as an unrenewable natural resource, have been an important support for the healthy development of economy and society. Minerals and rocks are always the main objects of geographical scientific research as the basic components of the crust. In the past few years, with a large amount of mineral resources being mined, there are less and less minerals that can be found on the surface [1]. A more efficient and accurate method is required to be explored to identify and classify minerals. To realize a wide area of the mineral resources investigation, and overcome some inconvenient transportation and natural conditions of mineral exploration, remote sensing technology, especially for hyperspectral remote sensing, has become a highly efficient and convenient method for detecting minerals.

The hyperspectral remote sensing, originated in the early 1980s, was one of the major technological breakthroughs in the field of land observation at the end of last century. It has led a new direction of remote sensing technology [2], [3]. Enabling the acquisition of data with increased number of spectral bands and higher spectral resolution, hyperspectral data have certainly given significant impacts on the land cover and land use classification [4].

In recent years, much work has been carried out to identify and classify minerals accurately by taking the advantage of hyperspectral data's narrow bandwidth and contiguous spectral [5]. The main classifiers include the spectral angle mapping (SAM) [6], the spectral feature fitting (SFF) [7], the orthogonal subspace projection (OSP) [8], [9], and the adaptive coherence/cosine estimator (ACE) [10]. The early unsupervised classification classifiers were also used on mineral identification, such as artificial neural network [11] and support vector machines [12], [13]. With the rapid development of machine learning, the deep learning [14], [15] and other classifiers have been developed continuously.

In fact, with these large numbers of classifiers, minerals and rocks' identification remains with several problems. First, mineral identification is mainly based on the spectral characteristics in the visible near-infrared (VNIR) bands in 0.4–2.5 μm, and these characteristics are related to certain chemical compositions and lattice structures of minerals and rocks [16], whereas the spectral absorption characteristics in the thermal infrared (TIR) bands always tend to be overlooked. Different types of minerals with various chemical compositions have their own typical spectral diagnosed characteristics in the given spectral region. For example, there are diagnosed characteristics in VNIR bands for iron oxide (Fe_mO_n), in shortwave infrared (SWIR) bands for hydroxide (–OH) functional group, and in the TIR bands for silicate ($–SiO_3$) and carbonate ($–CO_3$).

Manuscript received February 28, 2020; revised May 8, 2020; accepted May 20, 2020. Date of publication June 1, 2020; date of current version June 18, 2020. This work was supported in part by the Project of civil space technology pre-research of the 13th Five Year Plan under Grant D040104, and in part by the National Natural Science Foundation of China under Grant 41771398. *(Corresponding author: Honggen Xu.)*

Li Ni is with the Key Laboratory of Digital Earth Science, Aerospace Information Research Institute, Chinese Academy of Sciences, Beijing 100094, China (e-mail: nili@radi.ac.cn).

Honggen Xu is with the Wuhan Center of China Geological Survey, (Central South China Innovation Center for Geosciences), Wuhan 430205, China (e-mail: honggen_xu@163.com).

Xiaoming Zhou is with the School of Civil Engineering, Lanzhou University of Technology, Lanzhou 730050, China (e-mail: zhouxm0905@126.com).

Digital Object Identifier 10.1109/JSTARS.2020.2999057

Second, the alteration minerals contain a large number of Fe^{2+}, Fe^{3+}, OH–, $CO_3{}^{2-}$, and other ions or groups of ions. The electronic transition, vibration, and rotation of these ions make minerals display special spectral absorption and reflection characteristics in VNIR and SWIR bands [17]. Rocks are composed of different minerals and their spectral characteristics become much more complex [18].

Third, the vibration intensity of the minerals and rocks cannot be detected across the VNIR–SWIR bands even with hyperspectral data, which limits the ability of mineral indentation and classification. For example, most abundant minerals have special spectral characteristics in TIR bands in 8–14 μm [19]. The silicon–oxygen bond (Si–O) stretching vibrations in feldspars and quartz, as well as in other silicates, exhibit spectral characteristics in the TIR band. In addition, the TIR data can also provide some distinction characteristics amongst Al–OH, Mg–OH bearing minerals, carbonates, and so on [1]. In TIR bands, the radiance of the object mainly comes from itself [20], [21]. Most of the traditional research in TIR bands focuses on either the retrieval of land surface temperature [22], [23], emissivity [24], [25], soil moisture [26], and surface energy fluxes [27]. Obviously, the basis of mineral identification and classification in TIR bands is its emissivity [20].

To improve mineral identification and classification accuracy and realize fine mapping, some researches have evaluated different classifiers for mineral mapping by using just VNIR–SWIR and TIR data or the combination of those data [28]–[31]. It has been found that the combined data achieved a marked improvement compared to the results using either VNIR–SWIR or TIR data alone. The TIR data used by those researches are usually hyperspectral data with tens to hundreds of channels, in which the mineral features will be well captured. It is may not be a problem for airborne platforms because many sensors have this ability, such as the Thermal Airborne Spectrographic Imagery has 32 TIR channels, and the Spatially Enhanced Broadband Array Spectrograph System has 128 TIR channels. By contrast, the spaceborne sensor usually has a fewer TIR channels especially for sensors with spatial resolution higher than 100 m, such as ASTER has just five TIR channels. The limited spectral channels may influence the mapping accuracies; for example, there are fewer TIR channels to enhance the mineral features except silicates for ASTER [32]. The use for multispectral TIR data, especially for spaceborne sensor with less than ten channels, such as ASTER, has not been well studied. Whether or not, the spatial and spectral resolution will affect the mapping accuracies for those multispectral TIR sensors? This article tries to fully evaluate the effects of combination of the hyperspectral VNIR–SWIR reflectivity with the multispectral TIR emissivity on the accuracies of mineral identification and classification by using both simulated data and real data to answer this question. The sections in this article are organized as follows. The classification methodology is described in Section II. The data are described in Section III. The classification analysis for both simulated data and real data are analyzed in Section IV. Finally, conclusions are given in Sections V.

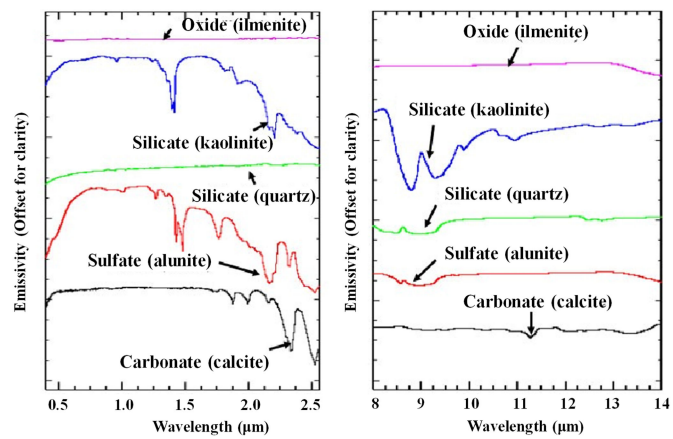

Fig. 1. Reflectivity and emissivity (offset for clarity) of typical minerals.

II. Methodology

A. Spectral Diagnosed Characteristics of Minerals in VNIR/SWIR/TIR

Different minerals have their own specific spectral features and characteristics in VNIR/SWIR/TIR bands, which are closely related to its intrinsic physical and chemical properties. Those special spectral absorption and reflection features and characteristics are reported to be the reason of the electronic transition, vibration, and rotation of ions. In 0.4–1.3 μm spectral band, the spectral features and characteristics are determined by the electronic transition of ions of Fe^{2+}, Fe^{3+}, Ni^{2+}, Cu^{2+}, and Mn^{2+}. In 1.3–2.5 μm spectral band, the spectral features and characteristics depend on $CO_3{}^{2-}$, OH^-, and $SO_4{}^{2-}$ ions. The silicon–oxygen bond (Si–O) stretching vibrations in feldspars and quartz, as well as in other silicates, exhibit spectral characteristics in the TIR region. Therefore, minerals containing these icons can be detected and identified by those spectral features and characteristics. The different spectral absorption and reflection features and characteristics in VNIR, SWIR, and TIR are shortly listed in Table I. Fig. 1 shows the reflectivity and emissivity of typical minerals, which also demonstrates the phenomena that different minerals have their own typical spectral characteristics in various spectral bands.

B. Review of Four Selected Classifiers

To evaluate how the accuracies of classification change when TIR data are introduced in mineral identification and classification, four traditional classifiers, i.e., SAM, SFF, OSP, and ACE, are used in the following experiment. Those four classifiers, which have been packaged as mapping methods in the ENVI (Environment for Visualizing Images) software, are famous and widely used in targeting minerals especially for hyperspectral data.

1) Spectral Angle Mapping (SAM): The SAM classifier is a classification method that uses N-dimensional angles to match the pixel spectrum and the reference spectrum [6]. It regards the spectrum as a multidimensional vector, and determines the

TABLE I
MINERALS IDENTIFIED IN DIFFERENT WAVELENGTH BANDS

Region	Wavelength range /μm	Minerals or groups of ions
VNIR	0.40-1.20	Fe, Mn and Ni oxide, hematite, goethite
SWIR	1.30-2.50	Hydrate, carbonate and sulfate
	1.47-1.82	Sulfates, such as alunite
	2.16-2.24	Minerals containing Al-OH groups of ions, such as kaolinite
	2.24-2.30	Minerals containing Fe-OH groups of ions, such as jarosite
	2.26-2.32	Carbonates, such as calcite, dolomite
	2.30-2.40	Minerals containing Mg-OH groups of ions, such as talc
TIR	8.00-14.0	Quartz, felspar, chalcedony, calcite, dolomite

similarity between the two spectra by calculating the general angle between the pixel spectral vector and the reference spectrum vector in the image. The smaller the angle, the more similar will be the two spectra. The spectral angle can be calculated as follows:

$$\theta = \cos^{-1}\frac{\sum_{i=1}^{n} t_i r_i}{\sqrt{\sum_{i=1}^{n} {t_i}^2}\sqrt{\sum_{i=1}^{n} {r_i}^2}} \tag{1}$$

where n is the number of bands, t_i is the pixel spectrum of the i band, and r_i is the reference spectrum of the i band. For the spectral angle independent of the modulus of the spectral vector, SAM could eliminate illumination effects in the different environment and emphasizes the similarity of the spectrum in shape.

2) Spectral Feature Fitting (SFF): SFF is one of the classifier nowadays used for spectral analysis about recognition and classification, which is based on spectral absorption features [7]. The envelope line of the test spectra and the reference spectra should be removed before spectra matching. Consequently, the curve of the test spectra and the reference spectra after the envelope line removal is fitted by least squares.

Due to the difference in the characteristic absorption depth of the test spectra and the reference spectra after the envelope line is removed, the curve shape of the reference spectra can be adjusted by adding a constant k to best fit and match the pixel spectrum; the calculation formula is as follows:

$$\rho' = \frac{\rho + k}{1 + k} \tag{2}$$

where ρ' is the transformed reference spectra, ρ is the original test spectra, and k is a constant not equal to –1.

The root-mean-square error (RMSE) is used to evaluate the matching degree of the two spectra. Each pixel spectrum can calculate a fitting value and an RMSE value relative to the reference spectrum. The pixel spectrum with a higher fitting value and a smaller RMSE value is considered to match the reference spectra. An SFF classifier is sensitive to the subtle mineral absorption features. Even the most subtle absorption features are highlighted. The recognition effect of SFF is better when the absorption characteristics of the spectral curve are obvious.

3) Orthogonal Subspace Projection (OSP): An OSP classifier is based on a linear spectral mixture model, which divides the mixed pixels into interest endmember (target) and noninterest endmember (background). The mineral is identified by enhancing the characteristics of the target and suppressing the background signatures [8]. According to the linear mixing model, the OSP model decomposes the endmember spectral matrix into target $d = m_1$ and background $U = [m_2, m_3, \ldots, m_k]$ as

$$r = d\alpha_1 + U\alpha_U + n. \tag{3}$$

To eliminate the feature vector of the background in the image, the data are projected onto the orthogonal complement matrix space of U, denoted as $P_U = I–U(U^TU)^{-1}U^T$, and the orthogonal space projection operator is obtained by maximizing the signal to noise ratio (SNR) principle as follows:

$$P_{OSP} = kP_{\mathrm{U}}d \tag{4}$$

where k is the normalization constant. On the one hand, this method can eliminate the influence of background spectral characteristics; on the other hand, it considers the maximization of residual signal under various noise conditions.

4) Adaptive Coherence/Cosine Estimator (ACE): An ACE classifier takes both the statistical model and subspace projection model into account. It assumes that the covariance structure of the background is the same regardless of the existence of the target. However, its variance is different, which directly affects the area proportion of the target in background [10]. The similarity between the test spectra and the reference spectra is determined by calculating the cosine square of the angle between two spectra. The formula is as follows:

$$D_{\mathrm{ACE}}(x) = \frac{x^T\hat{\Gamma}^{-1}D\left(D^T\hat{\Gamma}^{-1}D\right)^{-1}D^T\hat{\Gamma}^{-1}x}{x^T\hat{\Gamma}^{-1}x}. \tag{5}$$

Among them, x is the spectrum of the sample to be detected, $\hat{\Gamma}$ is the maximum-likelihood estimation of the background covariance matrix, and D is the target prior knowledge expression. Because this method is sensitive to noise, it is usually required to remove noise before target detection.

TABLE II
EIGHT MINERALS AND ROCKS USED TO GENERATE THE SIMULATED DATA

Category No.	Sample Name	Description
1	Alunite	Sulfate minerals
2	Calcite	Carbonate minerals
3	Kaolinite	Silicate minerals
4	Montmorillonite	Silicate minerals
5	Muscovite	Silicate minerals
6	Gneiss	Feldspar, quartz, mica
7	Marble	Calcite, dolomite
8	Quartz	Quartz

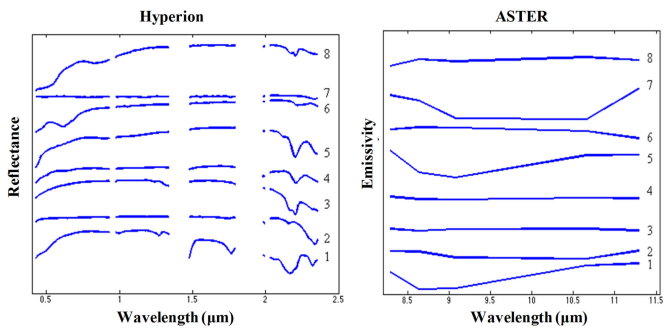

Fig. 2. Reflectivity and emissivity (offset for clarity) of eight targets (1—alunite, 2—calcite, 3—kaolinite, 4—montmorillonite, 5—muscovite, 6—gneiss, 7—marble, 8—quartz).

TABLE III
PROPORTION OF MIXED ENDMEMBER IN SEVEN DATASETS

Datasets No.	Soil	Category A	Category B
1	Not used	Not used	Not used
2	0-5%	Not used	Not used
3	0-5%	0-5%	0-5%
4	0-10%	0-10%	0-10%
5	0-10%	0-15%	0-15%
6	0-20%	0-20%	0-20%
7	0-20%	0-25%	0-25%

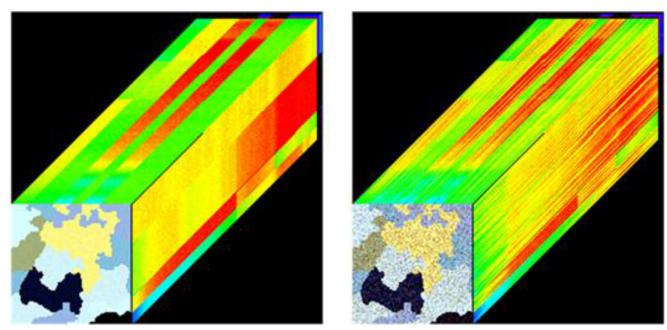

Fig. 3. 3-D cubes for the datasets 1 and 7 with eight targets in each dataset.

III. DATA

A. Simulated Data

Eight minerals and rocks were selected as the targets to be classified from the United States Geological Survey (USGS) Spectral Library and the Johns Hopkins University Spectral Library. The simulated data consisting of eight patches are generated with each patch corresponding to a kind of categories from the selected minerals and rocks. The corresponding information is listed in Table II.

Because the reflectivity and emissivity spectral curves measured by the hyperspectral Hyperion and multispectral ASTER are within a finite spectral bandwidth, the channel-effective reflectivity and emissivity according to the selected minerals and rocks are therefore a weighted average with the spectral response function as follows [20]:

$$X_{\mathrm{i}} = \frac{\int_{\lambda_1}^{\lambda_2} f_i(\lambda) X_\lambda d_\lambda}{\int_{\lambda_1}^{\lambda_2} f_i(\lambda) d_\lambda} \tag{6}$$

where X stands for the effective reflectivity and emissivity, $f_i(\lambda)$ is the spectral response function in channel i, and λ_1 and λ_2 are the lower and upper boundaries of the wavelength in channel i.

The Hyperion VNIR/SWIR data collect spectra in 242 continuous spectral channels covering the wavelength range from 0.356 to 2.578 μm, and 155 channels were considered according to the quality problem in the actual situation. The ASTER TIR data have five discrete TIR bands and cover the wavelength range from 8.125 to 11.65 μm. Fig. 2 shows the reflectivity in the Hyperion VNIR/SWIR band and the emissivity in ASTER TIR band of the eight targets, respectively. Those reflectivity and emissivity will be taken as the reference spectra in mineral identification and classification.

In order to simulate closer to the reality, the noise and mixture will be taken into account. The original category of each pixel is treated as ground truth. Both the white noises (bias is zero and standard deviation is 0.01) and the spectrum of soil and the spectrum of two random selected minerals in Table II are added to each pixel. In the process of spectral mixing, the linear spectral mixture model was used to generate the mixed reflectivity and emissivity spectra. The proportion of soil and the two random selected minerals are randomly determined and the maximum and minimum values are listed in Table III.

The sum of the proportions for the original category, the soil and two random selected minerals are equal to 1. Here, each dataset is also processed by considering spectra response function of Hyperion VNIR/SWIR data and ASTER TIR data. Finally, the seven different datasets with different mixture situations were generated. There were 160 channels in each datasets among which the first 155 channels are VNIR/SWIR reflectivity channels for Hyperion, and the last 5 channels are TIR emissivity for ASTER. Fig. 3 shows the 3-D cubes for the datasets 1 and 7 for demonstration purpose. Obviously, because of the higher mixing ratio in dataset 7, the simulated image shows more salt and pepper noise.

B. Real Data

In addition to the simulated data, the real data were also used to evaluate the effect of introducing TIR data in the mineral

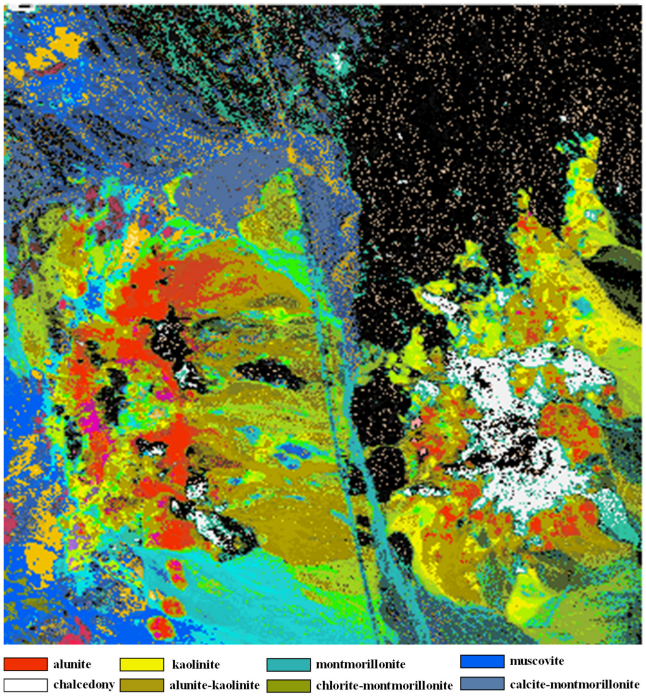

Fig. 4. Mineral distribution in studied area.

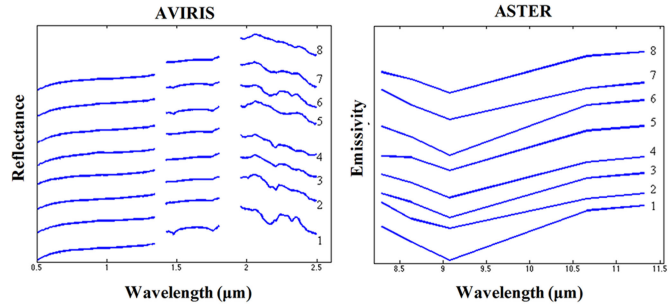

Fig. 5. Reflectivity and emissivity (offset for clarity) of eight targets (1—alunite, 2—kaolinite, 3—montmorillonite, 4—muscovite, 5—chalcedony, 6—alunite-kaolinite, 7—chlorite-montmorillonite, 8—calcite-montmorillonite).

identification and classification. The study area is the Cuprite in Nevada, USA. The Cuprite is a popular benchmarking dataset and extensively used for testing mineral identification and classification methods. The corresponding hyperspectral AVIRIS reflectivity data in VNIR/SWIR bands and the multispectral ASTER emissivity data in TIR bands were used. The AVIRIS VNIR/SWIR data were acquired on September 20, 2006 and the ASTER TIR data were acquired on August 15, 2006. The original AVIRIS VNIR/SWIR data have 224 channels ranging the wavelength from 0.37 to 2.48 μm. The VNIR/SWIR channels located in water absorptions zone and with too low SNR were removed from the original band set, and finally 170 VNIR/SWIR channels are left in our experiment. The original ASTER TIR data have five channels ranging the wavelength from 8.125 to 11.65 μm. In total, there are 175 channels for the joined spectrum from two separated different channels of AVIRIS VNIR/SWIR and ASTER TIR.

Because there is a spatial resolution difference between VIR/SWIR data (15.7 m) and TIR data (90 m), spatial registration is first carried out on TIR data to keep those two data in the same geographical coordinates with the same spatial resolution. There is extensive ground truth information available, which consists of 25 classes of minerals (see https://archive.usgs.gov/archive/sites/speclab.cr.usgs.gov/cuprite95.tgif.2.2um_map.gif). In consideration of the distribution of different minerals, a smaller dataset with the image size of 400 $\times$ 400 pixels was manually selected for our experiment. There are eight main minerals for this area including alunite, kaolinite, montmorillonite, muscovite, chalcedony, and so on. Fig. 4 shows the selected reference distribution of main minerals in the study area, which is tailored from the archive mineral map of USGS and will be used as the ground truth data for assessing classification accuracy. The black color indicated unclassified class. Because this mineral map was derived from analyzing the vibrational absorption features in minerals (typically in the 2–2.5 micron spectral region) common to OH^-, CO_3^-, and SO_4^- bearing minerals, a specific crystal structure, and subtle changes with the same ion affecting the identification results. In addition, other colors in Fig. 3 represent minerals other than the eight main minerals. Therefore, the salt- and pepper- like noise will appear in this figure. However, those noises appeared will not affect the analysis of the results because eight main minerals are taken into account.

Fig. 5 shows the reflectivities of selected minerals in the VNIR/SWIR band and the emissivity in the TIR band, respectively. Those spectra are gotten from the average spectra for each mineral in the ground truth data. Compared with the spectra in the simulated data (see Fig. 2), the spectral differences in both VNIR/SWIR band and TIR band are not obvious.

IV. Experimental Results

A. Classification Accuracies for Simulated Data

Four classifiers described above were used to classify the seven datasets of simulated data, which included the hyperspectral Hyperion data (H), the ASTER TIR data (A), and the combination of both (H&A). Figs. 6 and 7 show the OA of final classification results between the Hyperion data and the combination data, and those between the ASTER data and the combination data, respectively.

It can be found that the overall accuracies by using the multispectral ASTER TIR data alone are always lower than those by using the hyperspectral Hyperion VNIR/SWIR data alone. The classification accuracies are improved ranging from 4% to 13% for the selected four classifiers after introducing multispectral TIR data. The OA of ACE is higher, and the performance of other three classifiers are comparable. The accuracy of SFF is apparently not as good as those of three other classifiers when using hyperspectral VNIR/SWIR data alone. When the multispectral TIR data is introduced, the accuracy of SFF has been significantly increased, even obviously better than SAM.

Compared with using either VNIR/SWIR data or the TIR data, the overall accuracies are improved for all of datasets

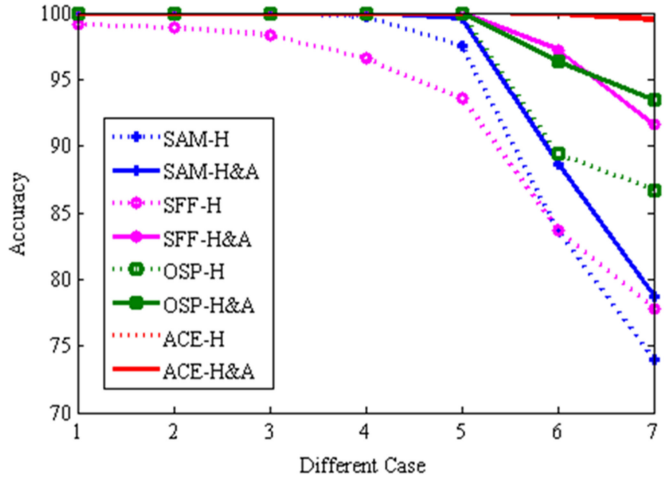

Fig. 6. Overall accuracy (OA) comparisons for different datasets. The dotted lines represent the classification accuracy for the Hyperion data alone, whereas the solid lines are for the combination of the Hyperion and ASTER data.

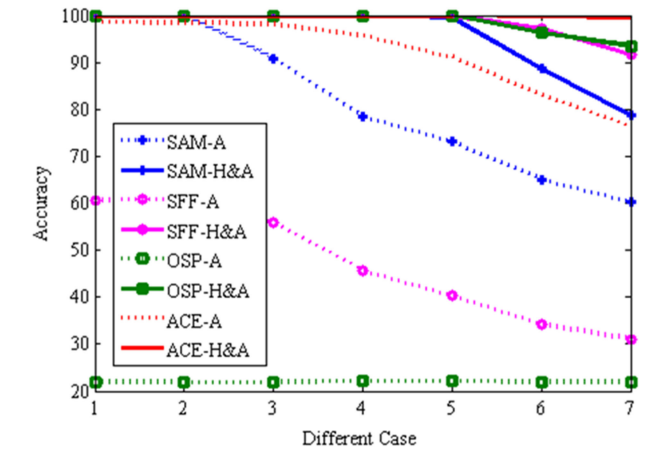

Fig. 7. OA comparisons for different datasets. The dotted lines represent the classification accuracy for the ASTER data alone, whereas the solid lines are for the combination of the Hyperion and ASTER data.

with the selected four classifiers when the combination of the VNIR/SWIR and TIR data are used together. The introduction of TIR assisting the classification with VNIR/SWIR makes an obvious improvement in overall accuracies. The classification accuracies by SFF increase the most, whereas those by ACE were not significantly improved. The improved accuracies for different classifiers under the different mixing conditions not only effectively prove the contribution of TIR data in classification, but also prove that the combining use of the hyperspectral VNIR/SWIR data and multispectral TIR data will increase the accuracy of mineral identification and classification.

Take the seventh simulated data for example, the confusion matrix is used to analyze the classification accuracy in detail. Fig. 8 shows the comparison of OA with the proposed four classifiers using hyperspectral VNIR/SWIR data, multispectral TIR data, and combination data. As shown in this figure, it is also found that the introduction of TIR data helps improve the accuracy of the SFF method mostly.

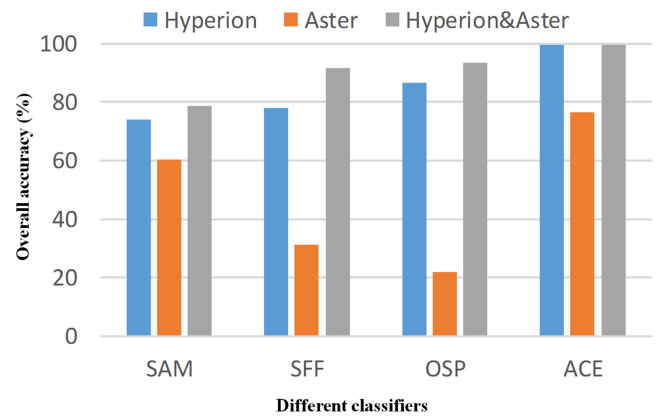

Fig. 8. OA comparisons for the selected seventh simulated data with different classifiers.

TABLE IV
CLASSIFICATION ACCURACIES OF DIFFERENT MINERALS USING FOUR CLASSIFIERS FOR THE SIMULATED DATA

	SAM				SFF			
	Hyperion		Combined		Hyperion		Combined	
OA	74.00		78.75		77.83		91.59	
Classes	Prod.	User	Prod.	User	Prod.	User	Prod.	User
1-ALU	77.38	100.00	80.71	100.00	87.69	100.00	82.71	100.00
2-CAL	69.36	93.21	71.28	86.82	15.98	100.00	89.38	96.93
3-KAO	89.13	86.01	89.22	87.55	88.08	98.98	89.35	98.80
4-MON	93.73	36.11	94.06	42.88	90.19	63.09	91.10	84.03
5-MUS	88.99	88.16	90.63	89.05	40.22	100.00	86.41	97.40
6-GNE	89.55	89.48	89.96	89.09	81.62	100.00	96.60	98.84
7-MAR	40.45	100.00	56.89	100.00	99.39	60.90	100.00	81.66
8-QUA	58.99	100.00	59.71	100.00	24.10	100.00	65.83	100.00

	OSP				ACE			
	Hyperion		Combined		Hyperion		Combined	
OA	86.70		93.43		99.57		99.50	
Classes	Prod.	User	Prod.	User	Prod.	User	Prod.	User
1-ALU	99.22	94.31	100.00	85.58	99.78	100.00	99.56	100.00
2-CAL	98.69	94.85	99.19	96.56	99.80	99.90	99.49	99.90
3-KAO	96.83	99.44	95.02	100.00	99.95	99.10	99.86	99.10
4-MON	99.92	82.67	86.56	100.00	99.59	99.75	99.59	99.92
5-MUS	75.82	100.00	97.69	99.58	97.28	100.00	98.10	100.00
6-GNE	100.00	56.78	100.00	72.60	99.51	99.84	99.43	100.00
7-MAR	57.38	100.00	85.98	100.00	100.00	99.31	100.00	98.87
8-QUA	92.45	93.80	93.88	99.62	97.48	100.00	95.68	100.00

Table IV list the OA of classification as well as detailed production and user accuracy of each kind of material for different classifiers. The classification accuracies of rocks are generally lower than those of other minerals, especially for marble and quartzite. The main reason is the mixture of several minerals in a rock. For example, the marble contains calcite, whereas the main compositions of quartzite are the same as those of gneiss. Therefore, the spectral difference between different kinds of rocks will become small. The classification accuracy of an SFF classifier improves the most with the introduction of TIR data, which plays a great role in improving the classification accuracy of calcite, muscovite, marble, and quartzite.

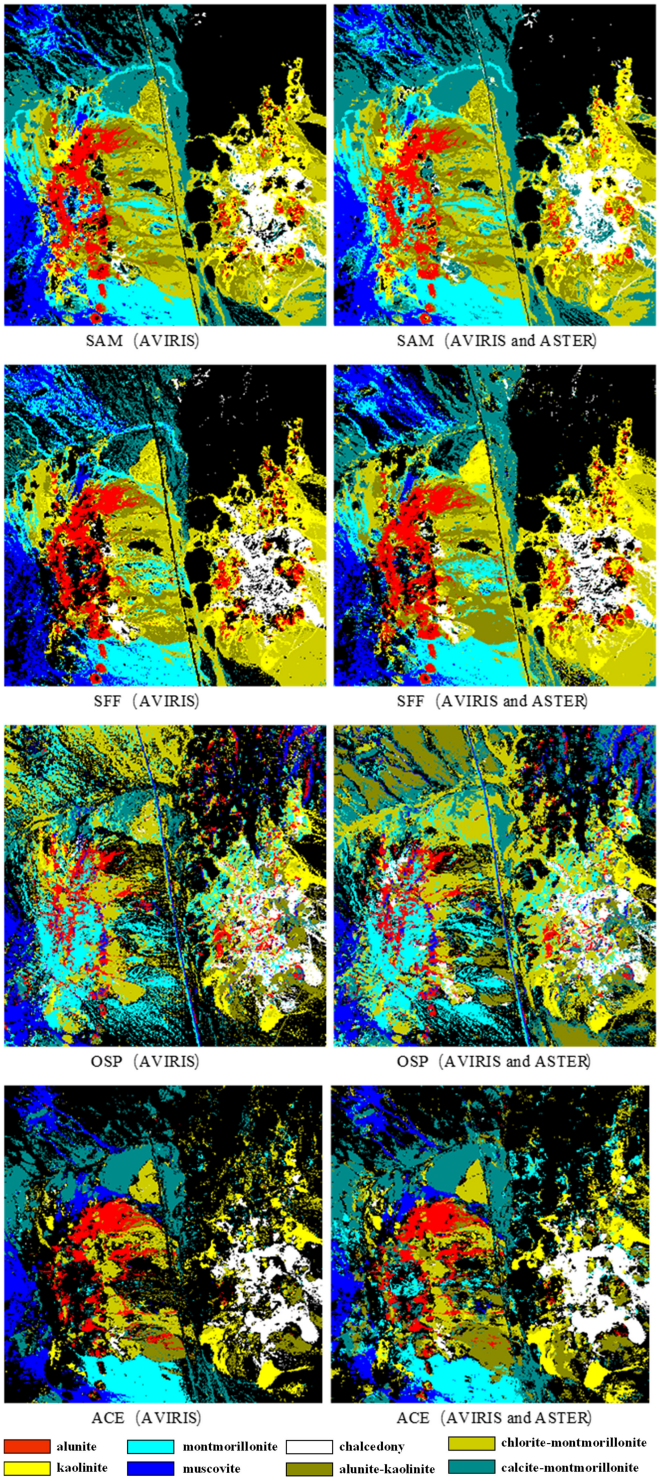

Fig. 9. Classification mapping results of minerals for the real data in Cuprite with different classifiers.

B. Classification Accuracies for Real Data

Four classifiers are also used to identify minerals with real AVIRIS data and the combination of AVIRIS and ASTER TIR data. The result of classification is shown in Fig. 9 and the accuracy of classification is shown in Table V. The black color in Fig. 9 indicated unclassified classes. The overall classification accuracies of those four classifiers are improved from 1% to 5%. Obviously, the most accurate classifier is SFF, followed by SAM and ACE, and the OSP classifier is not qualified.

TABLE V
CLASSIFICATION ACCURACIES OF DIFFERENT MINERALS USING FOUR CLASSIFIERS FOR THE REAL DATA

	SAM				SFF			
	AVIRIS		Combined		AVIRIS		Combined	
OA	79.27		80.10		81.43		84.59	
Kappa	0.76		0.77		0.78		0.82	
Classes	Prod.	User	Prod.	User	Prod.	User	Prod.	User
1-ALU	90.51	98.00	90.39	97.99	82.51	98.43	91.52	97.96
2-KAO	78.10	92.39	78.66	92.24	80.97	85.01	86.67	84.24
3-MON	89.53	92.77	90.53	94.95	85.46	87.47	93.37	80.26
4-MUS	89.73	98.84	92.45	99.19	68.88	93.83	77.64	98.09
5-CHA	79.75	100.00	80.68	100.00	86.42	100.00	82.88	100.00
6-ALU-KAO	44.84	54.86	46.45	56.57	84.30	89.29	85.84	92.42
7-CHL-MON	68.29	26.57	68.90	27.26	87.79	71.88	73.17	70.80
8-CAL-MON	96.59	56.24	96.59	57.52	68.80	100.00	68.94	95.82

	OSP				ACE			
	AVIRIS		Combined		AVIRIS		Combined	
OA	45.25		50.83		76.17		81.78	
Kappa	0.39		0.45		0.73		0.79	
Classes	Prod.	User	Prod.	User	Prod.	User	Prod.	User
1-ALU	47.82	78.15	50.75	85.00	61.13	88.35	67.64	95.94
2-KAO	76.79	97.63	74.09	97.07	89.38	96.77	92.64	98.81
3-MON	33.89	17.06	37.87	19.79	83.89	98.25	76.08	99.57
4-MUS	49.55	65.08	41.84	58.81	87.92	98.15	87.01	98.80
5-CHA	43.17	98.33	60.83	98.70	72.95	99.36	81.95	99.76
6-ALU-KAO	8.70	25.99	21.57	53.40	70.48	95.88	89.50	92.02
7-CHL-MON	46.34	17.82	53.66	21.10	68.90	56.22	66.77	77.94
8-CAL-MON	59.72	75.44	58.72	53.18	99.80	84.26	98.80	93.73

Because all kinds of minerals have almost similar spectral curve shown in Fig. 5 together with the effect of noise, it is difficult for the OSP classifier to accurately separate the target and the background after subspace projection transformation. Therefore, overall poor accuracies for various minerals are gotten in the OSP classifier. The ACE classifier is required to make minimum noise fraction (MNF) transformation to maximize the image SNR and then compare the target spectra with the background spectra, so the classification accuracy will be significantly improved. Furthermore, the spectra of minerals in the real data are nonlinearly mixed in VNIR/SWIR bands, and the classification accuracies of the OSP and ACE classifiers, which are designed with linear mixture consideration, would be reduced.

V. DISCUSSIONS

The abovementioned experiments proved that the spectral diagnosed characteristics in TIR region help identify and classify minerals. However, the degree of improving the accuracy is different for different datasets. The overall accuracies were improved about 4%–13% for the simulated data and about 1%–5% for the real data by using different classifiers. The reason for the improvement of classification accuracy is the obvious difference of reflectivity and emissivity spectra for the simulated data. As shown in Fig. 2, the shape of reflectivity and emissivity curves for different minerals are roughly different, together with the spectral absorption characteristics. Although the spectral differences between calcite and marble in VNIR/SWIR bands are slight, there are significant spectral emissivity absorption

characteristics in TIR bands between these two minerals. Fig. 2 shows that these minerals have their own significant absorption characteristics in TIR bands, especially for muscovite and marble, with which those minerals can be well identified.

Compared with the simulated data, the improvement of classification accuracy by introducing the TIR data is not obvious for the real data. The overall accuracies are just improved about 1%–5% by using different classifiers. The main reason may be the relative low spatial resolution of ASTER TIR data, where the spectral mixture of various minerals exists. It can be found in Fig. 5 that the similarity of each kind of mineral emissivity curves will affect the classification accuracies. In addition, the spectrum is linear mixed in the simulated data and spectrum mixture of minerals in the real data is nonlinear and complicated. Furthermore, the retrieval accuracies of emissivity in ASTER TIR bands are reported to be about 0.015 [21], which may not be satisfied with the required accuracies in classification.

Drawn from the simulated data and real data, the results will not be the same if those four classifiers are used in different datasets. The overall accuracies of different classifiers rely on the land classes in the study area, the training samples, and the noise in the observed spectra. Both SAM and SFF depend on spectral similarity between training samples and targets to be classified, SAM emphasizes on spectral shape, while SFF emphasizes on spectral absorption characteristics. For the real data, the differences in minerals' spectral shape are not obvious compared with the difference in spectral absorption, the overall accuracies of SFF are better than those of SAM. However, it is difficult for OSP and ACE classifiers to achieve a good accuracy when the sample spectrum is slightly different from that of the background.

In general, the introduction of TIR band helps to improve the classification accuracy, especially for some minerals with diagnostic features, such as quartz, felspar, chalcedony, calcite, dolomite, and so on. However, it is undeniable that if the spectral difference is very small and there is a large noise, the improvement of identification accuracy will be slight even if TIR band is introduced.

VI. Conclusion

This article analyses the spectral characteristics of the reflectivity spectra in VNIR/SWIR and the emissivity spectra in TIR for minerals. Both the simulated data and the real data have proven that the combination of hyperspectral VNIR-SWIR data and multispectral TIR data has a positive impact on the identification and classification of minerals.

To evaluate the effect of introducing the multispectral TIR data, seven datasets with different degrees of mixture of the minerals (such as kaolinite, alunite, calcite, quartz, and ilmenite) together with four classifiers, i.e., SAM, SFF, OSP, and ACE, were used in the simulated data. The classification accuracies for different classifiers are summarized and compared. The ACE classifier gets the most accurate classification, followed behind the OSP. The accuracies of SAM and SFF are slightly lower. However, the classification accuracies of four classifiers are improved ranging from 4% to 13% after introducing multispectral TIR data. Especially for the SFF method, its OA is increased about 13%, in which the identification accuracies of calcite, muscovite, marble, and quartzite has been obviously improved. The main reason is the apparent absorption characteristic differences of these minerals in TIR bands.

At the same time, the reflectivity of AVIRIS data and the emissivity of ASTER data in Cuprite, Nevada, USA, are also used in the real data experiment. With the different kinds of minerals, for example, alum, kaolinite, montmorillonite, muscovite, and chalcedony, four classifiers are also used to identify the effect of the combination of hyperspectral VNIR/SWIR data and multispectral TIR data. The overall classification accuracies of those four classifiers are improved from 1% to 5%. Some classifiers, such as ACE and SAM, show unobvious difference in classification accuracies because of the slight contrast between target and background spectra. It is obvious that the classification accuracy of real data is not excited compared with the simulated data. The possible reasons are summarized as follows.

1) The spatial resolution of ASTER TIR data is 90 m, which is much lower than expectation. It is easy to cause mixture pixels.
2) The retrieved accuracy of emissivity in TIR band and we argued what is the required accuracy of emissivity in classification. Apparently, the accuracy of retrieved emissivity directly affects the accuracy of classification.
3) The potential nonlinear mixture of mineral complicates the improvement of classification.

Although the classification improvement in the real data is not obvious, it is still shown that there is a good potential of introducing the multispectral TIR data. The multispectral TIR band data will be appropriate for mineral classification and mapping as the complementary of hyperspectral VNIR/SWIR data.

References

[1] G. Notesco *et al.*, "Mineral classification of land surface using multispectral LWIR and hyperspectral SWIR remote-sensing data. A case study over the Sokolov lignite open-pit mines, the czech republic," *Remote Sens.*, vol. 6, no. 8, pp. 7005–7025, Aug. 2014, doi: 10.3390/rs6087005.

[2] J. M. Bioucas-Dias, A. Plaza, G. Camps-Valls, P. Scheunders, N. Nasrabadi, and J. Chanussot, "Hyperspectral remote sensing data analysis and future challenges," *IEEE Geosci. Remote Sens. Mag.*, vol. 1, no. 2, pp. 6–36, Jun. 2013.

[3] Q. X. Tong, Y. Q. Xue, and L. F. Zhang, "Progress in hyperspectral remote sensing science and technology in china over the past three decades," *IEEE J. Sel. Topics Appl. Earth Observ. Remote Sens.*, vol. 7, no. 1, pp. 70–91, Jan. 2014.

[4] Y. G. Qian *et al.*, "Evaluation of temperature and emissivity retrieval using spectral smoothness method for low-emissivity materials," *IEEE J. Sel. Topics Appl. Earth Observ. Remote Sens.*, vol. 9, no. 9, pp. 4307–4315, Sep. 2016.

[5] R. N. Adep, A. Shetty, and H. Ramesh, "EXhype: A tool for mineral classification using hyperspectral data," *ISPRS J. Photogramm.*, vol. 124, pp. 106–118, Feb. 2017, doi: 10.1016/j.isprsjprs.2016.12.012.

[6] F. A. Kruse, A. B. Lefkoff, and J. B. Dietz, "Expert system-based mineral mapping in northern death valley, California/Nevada, using the airborne visible/infrared imaging spectrometer (AVIRIS)," *Remote Sens. Environ.*, vol. 44, no. 2/3, pp. 309–336, Jul. 1993, doi: 10.1016/0034-4257(93)90024-R.

[7] R. N. Clark, A. J. Gallagher, and G. A. Swayze, "Material absorption band depth mapping of imaging spectrometer data using a complete band shape least-squares fit with library reference spectra," in *Proc. 2nd Airborne Visible/Infrared Imag. Spectrometer Workshop*, Jan. 1990, vol. 2, pp. 4–5.

[8] J. C. Harsanyi and C. Chang, "Hyperspectral image classification and dimensionality reduction: An orthogonal subspace projection approach," *IEEE Geosci. Remote Sens. Mag.*, vol. 32, no. 4, pp. 779–785, Jul. 1994.

[9] C. I. Chang and A. Plaza, "A fast iterative algorithm for implementation of pixel purity index," *IEEE Geosci. Remote Sens. Mag.*, vol. 3, no. 1, pp. 63–67, Jan. 2006.

[10] S. Kraut and L. Scharf, "The CFAR adaptive subspace detector is a scale-invariant GLRT," *IEEE Trans. Signal Process.*, vol. 47, no. 9, pp. 2538–2541, Sep. 1999.

[11] B. A. Paya, I. I. Esat, and M. N. M. Badi, "Artificial neural network based fault diagnostics of rotating machinery using wavelet transforms as a preprocessor," *Mech. Syst. Signal Process.*, vol. 11, no. 5, pp. 751–765, Sep. 1997, doi: 10.1006/mssp.1997.0090.

[12] F. Melgani and L. Bruzzone, "Classification of hyperspectral remote sensing images with support vector machines," *IEEE Geosci. Remote Sens. Mag.*, vol. 42, no. 8, pp. 1778–1790, Sep. 2004.

[13] A. Maysam, G. H. Norouzi, and A. Bahroudi, "Support vector machine for multi-classification of mineral prospectivity areas," *Comput. Geosci.*, vol. 46, pp. 272–283, Sep. 2012, doi: 10.1016/j.cageo.2011.12.014.

[14] Y. S. Chen, Z. Lin, X. Zhao, G. Wang, and Y. Gu, "Deep learning-based classification of hyperspectral data," *IEEE J. Sel. Topics Appl. Earth Observ. Remote Sens.*, vol. 7, no. 6, pp. 2094–2107, Jun. 2014.

[15] A. Romero, C. Gatta, and G. Camps-Valls, "Unsupervised deep feature extraction for remote sensing image classification," *IEEE Geosci. Remote Sens. Mag.*, vol. 54, no. 3, pp. 1349–1362, Nov. 2015.

[16] E. A. Cloutis, "Review article hyperspectral geological remote sensing: Evaluation of analytical techniques," *Int. J. Remote Sens.*, vol. 17, no. 12, pp. 2215–2242, Aug. 1996, doi: 10.1080/01431169608948770.

[17] T. T. Zhang, F. Liu, "Application of hyperspectral remote sensing in mineral identification and mapping," in *Proc. 2nd Int. Conf. Comput. Sci. Netw. Technol.*, 2012, pp. 103–106.

[18] N. Gila, O. Yaron, and B. D. Eval, "Integration of hyperspectral short-wave and longwave infrared remote-sensing data for mineral mapping of Makhtesh Ramon in Israel," *Remote Sens.*, vol. 8, no. 4, Apr. 2016, Art. no. 318, doi: 10.3390/rs8040318.

[19] C. A. Bishop, J. G. Liu, and P. J. Mason, "Hyperspectral remote sensing for mineral exploration in Pulang, Yunnan Province, China," *Int. J. Remote Sens.*, vol. 32, no. 9, pp. 2409–2426, May 2011, doi: 10.1080/01431161003698336.

[20] Z. L. Li *et al.*, "Satellite-derived land surface temperature: Current status and perspectives," *Remote Sens. Environ.*, vol. 131, pp. 14–37, Apr. 2013, doi: 10.1016/j.rse.2012.12.008.

[21] S. B. Duan *et al.*, "Validation of collection 6 MODIS land surface temperature product using in situ measurements," *Remote Sens. Environ.*, vol. 225, pp. 16–29, May 2019, doi: 10.1016/j.rse.2019.02.020.

[22] S. B. Duan, Z. L. Li, and P. Leng, "A framework for the retrieval of all-weather land surface temperature at a high spatial resolution from polar-orbiting thermal infrared and passive microwave data," *Remote Sens. Environ.*, vol. 195, pp. 107–117, Jun. 2017, doi: 10.1016/j.rse.2017.04.008.

[23] S. B. Duan, Z. L. Li, B. H. Tang, H. Wu, and R. L. Tang, "Generation of a time-consistent land surface temperature product from MODIS data," *Remote Sens. Environ.*, vol. 140, pp. 339–349, Jan. 2014, doi: 10.1016/j.rse.2013.09.003.

[24] Y. G. Qian, S. Qiu, N. Wang, X. Kong, H. Wu, and L. Ma, "Land surface temperature and emissivity retrieval from time-series mid-infrared and thermal infrared data of SVISSR/FY-2C," *IEEE J. Sel. Topics Appl. Earth Observ. Remote Sens.*, vol. 6, no. 3, pp. 1552–1563, Jun. 2013.

[25] C. X. Gao, Z. L. Li, S. Qiu, B. H. Tang, H. Wu, and X. G. Jiang, "An improved algorithm for retrieving land surface emissivity and temperature from MSG-2/SEVIRI data," *IEEE Geosci. Remote Sens. Mag.*, vol. 52, no. 6, pp. 3175–3191, Jun. 2014.

[26] W. Zhao, A. Li, H. Jin, Z. Zhang, J. Bian, and G. Yin, "Performance evaluation of the triangle-based empirical soil moisture relationship models based on Landsat-5 TM data and in situ measurements," *IEEE Geosci. Remote Sens. Mag.*, vol. 55, no. 5, pp. 2632–2645, May 2017.

[27] W. Zhao, A. Li, and W. Deng, "Surface energy fluxes estimation over the South Asia subcontinent through assimilating MODIS/TERRA satellite data with *in situ* observations and GLDAS product by SEBS model," *IEEE J. Sel. Topics Appl. Earth Observ. Remote Sens.*, vol. 7, no. 9, pp. 3704–3712, Sep. 2014.

[28] M. Black, T. R. Riley, G. Ferrier, A. H. Fleming and P. T. Fretwell, "Automated lithological mapping using airborne hyperspectral thermal infrared data: A case study from Anchorage Island, Antarctica," *Remote Sens. Environ.*, vol. 176, pp. 225–241, Apr. 2016, doi: 10.1016/j.rse.2016.01.022.

[29] X. Chen, T. A. Warner, and D. J. Campagna, "Integrating visible, near-infrared and short wave infrared hyperspectral and multispectral thermal imagery for geologic mapping: Simulated data," *Int. J. Remote Sens.*, vol. 28, no. 11, pp. 2415–2430, 2007, doi: 10.1080/01431160600702624.

[30] X. Chen, T. A. Warner, and D. J. Campagna, "Integrating visible, near-infrared and short-wave infrared hyperspectral and multispectral thermal imagery for geological mapping at Cuprite, Nevada," *Remote Sens. Environ.*, vol. 110, no. 3, pp. 344–356, Oct. 2007, doi: 10.1016/j.rse.2007.03.015.

[31] J. L. Feng, D. Rogge, and B. Rivard, "Comparison of lithological mapping results from airborne hyperspectral VNIR-SWIR, LWIR and combined data," *Int. J. Appl. Earth Observ.*, vol. 64, pp. 340–353, Feb. 2018, doi: 10.1016/j.jag.2017.03.003.

[32] F. D. Van Der Meer *et al.*, "Multi- and hyperspectral geologic remote sensing: A review," *Int. J. Appl. Earth Observ.*, vol. 14, no. 1, pp. 112–128, Feb. 2012, doi: 10.1016/j.jag.2011.08.002.

Li Ni received the Ph.D. degree in cartography and geographical information system from the Institute of Remote Sensing and Digital Earth, Chinese Academy of Sciences, Beijing, China, in 2015.

She is currently an Associate Researcher with the Aerospace Information Research Institute, Chinese Academy of Sciences. Her research interests include the land surface temperature retrieval and application of hyperspectral remote sensing.

Honggen Xu received the B.S. and Ph.D. degrees in photogrammetric engineering and remote sensing from Wuhan University, Wuhan, China, in 2003 and 2008.

He is currently a Senior Engineer with Wuhan Center of China Geological Survey (Central South China Innovation Center for Geosciences), Wuhan, China. His research interests include remote sensing data processing and application of hyperspectral remote sensing.

Xiaoming Zhou received the Ph.D. degree in cartography and geographical information system from the Institute of Geographic Sciences and Natural Resources Research, Chinese Academy of Sciences, Beijing, China, in 2015.

He is currently an Associate Professor with the Lanzhou University of Technology, Lanzhou, China. His research focuses on the thermal infrared remote sensing and application of remote sensing.